RSC Advances

PAPER

View Article Online
View Journal | View Issue

Cite this: *RSC Adv.*, 2021, **11**, 22264

Electronic and optical properties of orthorhombic $(CH_3NH_3)BX_3$ (B = Sn, Pb; X = F, Cl, Br, I) perovskites: a first-principles investigation†

Sean Nations,[ab] Ting Jia,[a] Shengnian Wang*[b] and Yuhua Duan *[a]

Lead halide perovskites have generated considerable interest in solar cell, sensor, and electronics applications. While great focus has been placed on $(CH_3NH_3)PbI_3$, an organic–inorganic hybrid perovskite, comparatively little work has been done to understand some of its existing crystal phases and analogous materials after substituting with Sn and/or other halogens in the framework. Here, first-principles density functional theory calculations are performed to comprehensively evaluate the electronic and optical properties of $(CH_3NH_3)BX_3$ (B = Sn, Pb; X = F, Cl, Br, I) in a low-temperature orthorhombic phase. Bulk modulus, electronic structures, and several optical properties of these perovskite systems are further calculated. The obtained results are first confirmed by comparing with existing perovskite systems in literature. The shifting trends on those physical properties when extending to other barely studied systems of $(CH_3NH_3)BX_3$ is further revealed. The band gap of these perovskites is found to decrease when varying halogen anion in "X" sites from F to I, and/or substituting Pb cations with Sn in "B" sites. Notably, the less toxic Sn-containing perovskites, $(CH_3NH_3)SnI_3$ in particular, display higher absorption coefficients in the visible light range than their Pb-containing counterparts. An orthorhombic $(CH_3NH_3)PbF_3$ is predicted to exist at low temperature, and adsorb strongly UV energy. Our systematical examination efforts on the two groups of perovskites provide valuable physical insights in these materials, and the accompanied new findings warrant further investigation on such subjects.

Received 27th February 2021
Accepted 12th June 2021

DOI: 10.1039/d1ra01586a

rsc.li/rsc-advances

1. Introduction

There is an ever-increasing environmental and social need to reduce carbon emissions which originate largely from fossil fuel burning. Utilizing clean and abundant solar energy by photovoltaic technologies is one major effort scientists are working on to accomplish these missions. Although silicon-based photovoltaic dominates current market share with an efficiency as high as ~21%, perovskites-based photovoltaics (PVs) demonstrates the fastest improvement on power conversion efficiency (PCE) in single-junction solar cells, reaching 25.2% in only ten years. Besides their promising PCE, perovskite thin films can be easily synthesized and integrated into devices and the prepared PVs also can tolerate much higher defect concentration than their Si-based counterparts. Besides their promising long-term solution to the climate crisis, perovskite materials can also play important roles in short-term solutions that make the current fossil fuel dominated energy supply greener.[1–5] For example, the maintenance of appropriate fuel-to-air ratio can not only maximize combustion efficiency of fossil fuels, but also minimize the emission of toxic gases such as NO_x to the environment. This requires gas sensors suitable for extreme environmental conditions (temperature, pressure, and potential exposure to free radicals).[6] The semiconductive and tunable optical properties of perovskite materials grant them interests as optical and photoelectrochemical sensors in combustion processes to detect ppm-range NO_x signal in emission gas at high-temperature.[7–9]

In a common metal halide perovskites structure, ABX_3, A is an organic (*e.g.*, methyl ammonium and formamidinium) or inorganic cation (*e.g.*, cesium), B is a metal cation such as lead, and X is a halogen anion. One big drawback of such perovskite materials lies on the involvement of lead, which causes safety concerns during synthesis and applications. With similar valence electrons for bonding, tin is considered as a potential replacement for lead in the metal halide perovskite structure to mitigate toxicity.[10] Another challenge in perovskite applications comes from their short storage and operation lifetime. Perovskites face great stability and degradation issues when exposed to environmental (*e.g.*, moisture, oxygen, and ultraviolet light), accompanied with consequent hygroscopicity, thermal instability, and ion migration issues.[4] Different degradation mechanisms are proposed, and great efforts have been made for their mitigations or solutions. One effective strategy is to replace elements in the ABX_3 structure of perovskite by partially

[a]*National Energy Technology Laboratory, United States Department of Energy, Pittsburgh, Pennsylvania 15236, USA. E-mail: yuhua.duan@netl.doe.gov*
[b]*Chemical Engineering Department, Louisiana Tech, University, Ruston, Louisiana 71272, USA. E-mail: swang@latech.edu*

† Electronic supplementary information (ESI) available. See DOI: 10.1039/d1ra01586a

substituting some majority halogen and/or metal ions or using their mixture, which could not only alleviate those stability issues, but also finely tune the electronic and optical properties of the perovskite crystals.[11] For example, as the A site in perovskites is typically occupied by a larger cation than the B site, Pb and Sn containing perovskites normally have the A site occupied by these relatively large metal atoms. However, by selection of a comparatively large organic cation, the metal can be made to occupy the B position.[1] An abnormally high absorption coefficient in the visible light range allows the material to function as a thin absorbing layer in photovoltaic cells to mitigate efficiency loss occurring mainly due to electron–hole recombination. These results have fueled hopes in perovskite applications and interests in new physical insights on the roles different metal and halide ions play in perovskite structure.[1–5]

Another effective strategy comes from the retention of stable phases of perovskite crystals. Depending on the temperature, (MA)BX_3 (MA = CH_3NH_3; B = Sn, Pb; X = Cl, Br, I) perovskites exist in several different phases.[12–14] At high temperatures, they are in the cubic phase ($Pm\bar{3}m$). For example, the transition temperatures of (MA)PbX_3 (X = Cl, Br, I) are 177 K, 236 K, and 330 K respectively. Below these temperatures, (MA)PbX_3 perovskites stay in the tetragonal phase ($I4/mcm$). Under further low temperatures (*i.e.*, below 172 K, 149–154 K, and 161 K for (MA)PbX_3 (X = Cl, Br, I respectively)), these perovskites are in the form of an orthorhombic phase (*Pnma*).[12] In the literature, the electronic and optical properties of the high-temperature cubic phase (MA)BX_3 (B = Sn, Pb; X = Cl, Br, I) were widely studied both by computational calculations and experimental measurements.[5,15–31] However, few studies look into these perovskites in their low-temperature phases, particularly the orthorhombic phase. One possible reason lies in the fact that many of these structures may only be stable at very low temperatures. Employing density functional theory (DFT), Ali *et al.*[17] explored the structural, mechanical, electronic, and thermoelectric properties of the low-temperature orthorhombic perovskite phase of (MA)PbI_3. They obtained a 1.57 eV band gap for (MA)PbI_3 and found its lattice thermal conductivity is anisotropic, and the lattice thermal conductivity at 150 K was found to be 0.189, 0.138, and 0.530 W m^{-1} K^{-1} along the *a*, *b*, and *c* directions; however, there was no reporting on its optical properties. Using the non-local optB86b + vdWDF functional, Wang *et al.*[32] predicted the crystal structure and band gap of (MA)PbI_3 in excellent agreement with experimental data. Using HSE06 hybrid functional approach, Feng and Xiao[33] explored the effective masses and electronic and optical properties of orthorhombic (MA)SnX_3 (X = Cl, Br, and I) as solar energy absorbers. Their results indicated that both the effective masses and band gaps of (MA)SnX_3 perovskites decrease when the "X" sites change from chlorine to iodine, but their optical dielectric constants do not go down monotonically. No report was yet found in the literature on the structures and optical properties of (MA)BF_3 (B = Sn, Pb). Hence, a question arises if such structures could exist, even at low temperatures. Before we could evaluate the performance of perovskites (MA)BX_3 (MA = CH_3NH_3; B = Sn, Pb; X = F, Cl, Br, I) as either solar cell or sensor candidate materials, much work is still needed to be done to understand the electronic and optical properties of these perovskites in their stable phases at different temperatures. In this study, we performed extensive investigations on the electronic and optical properties of perovskite crystals of (MA)BX_3 in the low-temperature orthorhombic phase and make comparisons with the corresponding phases stable in high temperatures. This study serves as the first step to evaluate this organic–inorganic hybrid halide perovskite group in low-temperature phase to provide physical insights on their potentials.

2. Theoretical methods

Calculations here were performed *via* first-principles density functional theory (DFT), accomplished *via* the Vienna *ab initio* simulation package (VASP),[34–36] using the plane-wave basis set and projector-augmented wave (PAW) method.[37] Exchange and correlation effects were taken into account in a generalized gradient approximation (GGA) by Perdew–Burke–Ernzerhof (PBE) functional.[38] The cutoff energy for plan waves was 520 eV and the electronic energy convergence was set to 10^{-4} eV. As shown in Fig. 1, the unit cells of the orthorhombic phase ($Z = 4$) with space group *Pnma* (#62) were used to model all eight structures. *K*-point sampling grid of 9 × 6 × 9 was used to sample the (MA)PbX_3 and (MA)SnX_3 perovskites. The ionic positions were relaxed until the Hellmann–Feynman force on each atom was less than 0.01 eV $Å^{-1}$.

3. Results and discussion

3.1 Geometric and mechanical properties

The structures of (MA)BX_3 were first relaxed geometrically by minimizing their energies. We performed the optimizations for

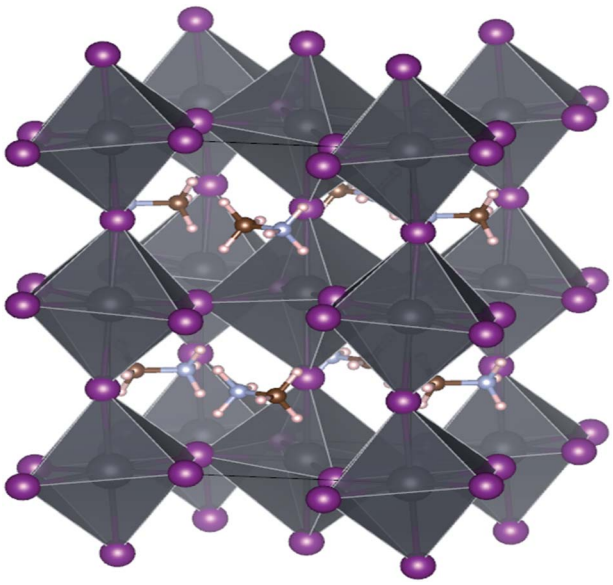

Fig. 1 The unit cell of (CH_3NH_3)BX_3 (B = Sn, Pb, X = F, Cl, Br, I) with *Pnma* (#62) nspace symmetry. Pink spheres are hydrogen atoms, brown ones are for carbon, light gray for nitrogen, purple for halides, and dark gray for metal Sn or Pb.

Table 1 The optimized crystal structures and volumes of orthorhombic (MA)BX_3 (B = Sn, Pb; X = F, Cl, Br, I) perovskites

Perovskite	a (Å)	b (Å)	c (Å)	V (Å^3)	E (eV per formula unit)
(MA)SnF_3	6.3623	9.6369	7.4482	456.67	−59.13799
(MA)$SnCl_3$	7.5518 (7.550)[a]	11.3363 (11.067)[a]	8.4178 (7.905)[a]	720.64 (660.5)[a]	−54.21088
(MA)$SnBr_3$	7.9478 (7.813)[a]	11.8729 (11.546)[a]	8.7304 (8.144)[a]	823.83 (734.7)[a]	−52.58994
(MA)SnI_3	8.5025 (8.326)[a]	12.6634 (12.428)[a]	9.1863 (8.556)[a]	989.10 (885.4)[a]	−50.82122
(MA)PbF_3	6.3889	9.8163	7.5376	472.72	−59.39415
(MA)$PbCl_3$	7.6084	11.5334	8.5153	747.23	−54.41641
(MA)$PbBr_3$	8.0029	12.0780	8.8423	854.70	−52.75472
(MA)PbI_3	8.5536 (8.5551)[b] (8.581)[c] (8.557)[d]	12.9027 (12.5804)[b] (12.908)[c] (12.964)[d]	9.2975 (8.8362)[b] (9.346)[c] (9.250)[d]	1026.12	−50.94207

[a] From ref. 40. [b] From ref. 1. [c] From ref. 17. [d] From ref. 39.

Pnma (#62) symmetries of (MA)BX_3 with the received crystal constants listed in Table 1. While studies of some individual perovskites of those or others that contain a mixture of two halogens can be found in scattered literature, a comprehensive comparison between the perovskites in this class is yet available to reveal trends in their physical properties with various halogen and/or metal substitutions. In contrast to the rich available data for the cubic phase of this halide perovskite family which has been published in the literatures,[5,12,15,16,18–31] only a few computational studies focus on the orthorhombic phase of (MA)PbI_3 and (MA)SnX_3 (X = Cl, Br, and I).[1,17,32,33] As an example, Table 2 lists our optimized atomic fractional coordinates of $MAPbI_3$ in comparison with the reported structures in Materials Project,[39] while the optimized atomic coordinates of the rest of the seven structures of (MA)BX_3 are provided in Tables S1–S7 of the ESI.† Overall, as one can see from Tables 1, 2 and S1–S7,† our optimized structures of (MA)BX_3 are in good agreement with available experimental data and other theoretical modeling results. For (MA)SnX_3 (X = Cl, Br, I), our optimized crystal constants and volumes are slightly bigger than those calculated by HSE06 functional.[33] For (MA)PbI_3, our geometry simulation results (Tables 1 and 2) agree well with that of using PBE.[17,39] However, the PBEsol appears to better approximate the b and c lattice constants as compared to the experimental results, though it is outperformed by PBE for the a lattice constant.[17] For the available Sn-containing perovskite sources, the Grimme van der Waals correction was used to account for the dispersion interactions, resulting in lower lattice constants than ours.[32,33] This lack of dispersion interaction correction and the precision of exchange-correlation functional (PBE over HSE06) likely explain the systematic over-estimation of lattice constants in our results. But when focusing on trends of crystal structure changes with different halogen anions, larger halogens lead to more volume expansion of the crystal framework in the orthorhombic phase perovskites as expected. As the consequence, a decreased band gap is found with their values becoming more favorable to the adsorption of visible light (a rationale for this behavior being laid out in Section 3.2). Similar trends are also found when large metal element (*e.g.*, Pb over Sn) occupy the B sites of (MA)BX_3. However, such changes are more pronounced when varying halogen anions in the X sites of the perovskite structure.

Fig. 2 displays the total energy *versus* volume change for (MA)PbX_3 (X = F, Cl, Br, I) perovskites. The corresponding data for (MA)SnX_3 (X = F, Cl, Br, I) are provided in Fig. S1 of the ESI.† For either Pb or Sn in the B sites, the perovskites involving smaller halogen anions have a significantly higher change rate of the total energy with respect to volume near the minimum energy,

Table 2 The calculated fractional coordinates of atoms in orthorhombic (MA)PbI_3. The corresponding data from Materials Project[39] are given in brackets for comparison

	Fractional coordinates		
Element	x	y	z
H	0.4977 (0.4943)	0.3151 (0.3146)	0.858 (0.8570)
H	0.4905 (0.4948)	0.3197 (0.3192)	0.119 (0.1201)
H	0.3395 (0.3381)	0.2500 (0.2500)	0.9198 (0.9214)
H	0.6576 (0.6598)	0.2500 (0.2500)	0.0526 (0.0503)
C	0.5300 (0.5324)	0.2500 (0.2500)	0.0624 (0.0622)
N	0.4610 (0.4596)	0.2500 (0.2500)	0.9149 (0.9151)
I	0.8096 (0.8161)	0.9755 (0.9779)	0.3012 (0.3072)
I	0.5404 (0.5377)	0.2500 (0.2500)	0.4846 (0.4874)
Pb	0.5000 (0.5000)	0.0000 (0.0000)	0.5000 (0.5000)

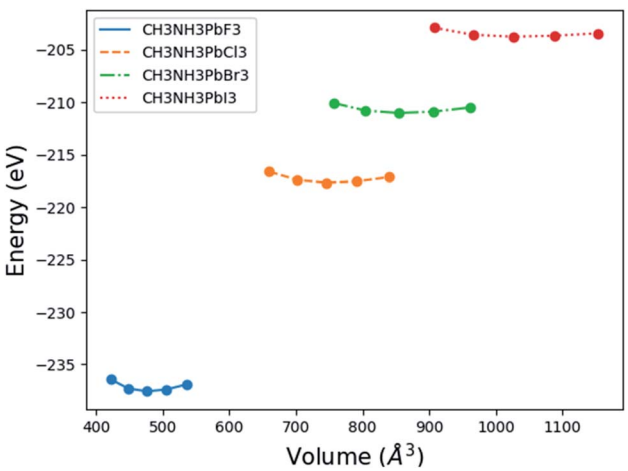

Fig. 2 Energy *versus* volume for (MA)PbX_3 perovskites.

Table 3 The fitted parameters (B_0, B'_0) and bulk modulus (B) of (MA)BX_3 by fitting to the Birch–Murnaghan equation of state (E–V)

Perovskite	B_0 (eV Å^{-3})	B'_0 (dimensionless)	B (GPa)	R^2 (dimensionless)
(MA)SNF_3	0.29533	6.02412	32.0	1.0000
(MA)$SNCL_3$	0.21958	6.75097	24.0	0.9998
(MA)$SNBR_3$	0.18370	7.06354	20.2	0.9998
(MA)SNI_3	0.26958	4.85373	29.1	1.0000
(MA)PBF_3	0.18086	6.74740	19.9	1.0000
(MA)$PBCL_3$	0.13778	6.57428	15.3	0.9999
(MA)$PBBR_3$	0.11688	6.30812	13.1	0.9999
(MA)PBI_3	0.13023	11.24429	15.0 (15.45)[a]	0.9983

[a] From ref. 17.

indicating a higher bulk modulus. This is confirmed by fitting the simulation data of the total energy (E) *versus* volume (V) in the form of Birch–Murnaghan equation of states (EOS) using eqn (1),

$$E(V) = E_0 + \frac{9 \times B_0 V_0}{16}\left\{\left[\left[\left(\frac{V_0}{V}\right)^{\frac{2}{3}} - 1\right]^3 \times B'_0 + \left[\left[\left(\frac{V_0}{V}\right)^{\frac{2}{3}} - 1\right]^2 \times \left[6 - 4 \times \left(\frac{V_0}{V}\right)^{\frac{2}{3}}\right]\right]\right\} \quad (1)$$

where a subscript of 0 indicates the equilibrium value of that parameter. B_0 refers to the base-level bulk modulus, with B'_0 referring to the first order variation of the bulk modulus, B, with pressure, P, all according to eqn (2). P is taken to be 1 atm.

$$B = B_0 + B'_0 \times P \quad (2)$$

The received parameters are listed in Table 3, together with the coefficients of determination of the regression fitting of the EOS models in those systems. Besides minimum fitting error, our bulk modulus result for (MA)PbI_3 (15 GPa) agrees well with the only available literature data (15.45 GPa in ref. 17). As halogen anion varies from F to Br in the X sites, the bulk modulus of perovskites decreases, which is consistent with observations from others. This can be attributed to the reduction of electronegativity when large halogen anions are present in the crystal. Smaller halogen anions in the X sites of perovskites provide larger resistance to the volume change, particularly to compression, as compared to larger halogens, due to the stronger interactions between protons and electrons. Such energy upshift from the equilibrium state is reflected in the fitting values of the bulk modulus change listed in Table 3. As for Sn and Pb in the B sites of the crystal structure, Sn-containing perovskites carry higher bulk moduli. The presence of f-orbitals in Pb's electronic configuration may enable more occupiable states for electrons. The changes of B_0 values in our results reflect such lower energy deviations with an increase in pressure, while an outlier exists for I-containing perovskites, which have significantly different B'_0 values than the other six perovskites examined.

3.2 Electronic structure properties

Due to the DFT approximations, which underestimate the excited state energies, the calculated band gap is usually smaller than the experimental measurement.[41] The beyond-DFT methods are usually used to amend such band gap underestimations. As shown in Table 4, with the HSE06 functional approach, Feng and Xiao[33,40] obtained larger band gaps of (MA)SnX_3 (X = Cl, Br, I). With inclusion of the GW many-body correction, Chiarella *et al.*[42] calculated the band gaps of the cubic phase of two Sn-containing perovskites ((MA)$SnCl_3$: 3.44 eV; (MA)$SnBr_3$: 1.90 eV), which are relatively close to the experimental measured values of 3.69 eV and 2.15 eV respectively.[43] Besides, Lang *et al.*[5] reported that the spin-orbital

Table 4 The calculated band gaps (E_{gap}: without including SOC, SOC_E_{gap}: with including SOC) and the formation energies (E_{form}) of orthorhombic (MA)BX_3 (B = Sn, Pb; X = F, Cl, Br, I) perovskites

Perovskites	E_{gap} (eV)	SOC E_{gap} (eV)	E_{form} (eV per formula unit)
(MA)SnF_3	2.325	2.122	0.11890
(MA)$SnCl_3$	1.494 (1.94)[a] (2.8)[b]	1.193	−0.16782
(MA)$SnBr_3$	1.186 (1.04)[a] (2.0)[b]	0.804	−0.18245
(MA)SnI_3	0.969 (1.7)[b]	0.520	−0.12346
(MA)PbF_3	3.466	2.651	−0.17052
(MA)$PbCl_3$	2.685	1.614	−0.20019
(MA)$PbBr_3$	2.265 (2.3)[c]	1.171	−0.18966
(MA)PbI_3	2.030 (1.61)[d] (1.80)[e] (1.76)[f]	0.808	−0.14134

[a] From ref. 42. [b] From ref. 33. [c] From ref. 16. [d] From ref. 1. [e] From ref. 17. [f] From ref. 39.

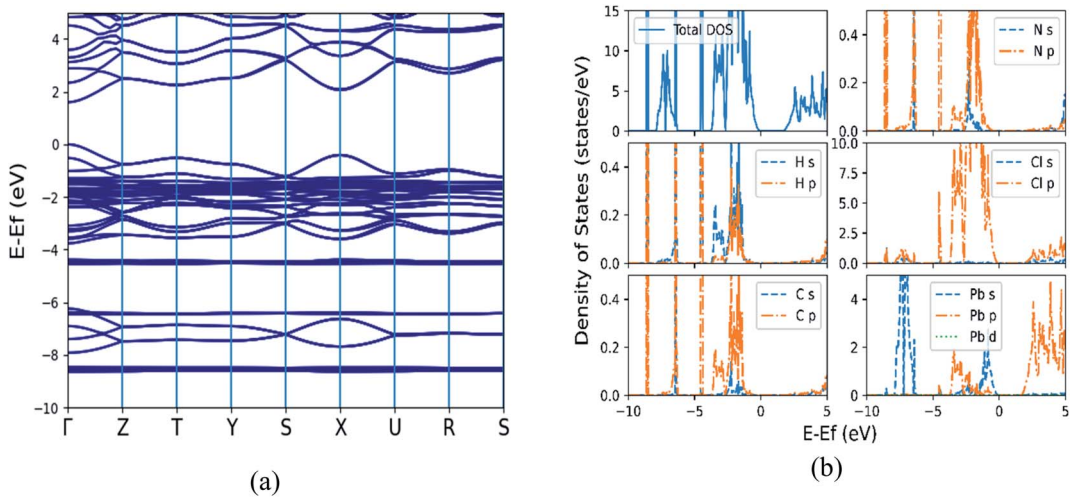

Fig. 3 The calculated electronic structural properties for (MA)$PbCl_3$ by including spin orbit coupling (SOC). (a) Band structure with a direct band gap of 1.614 eV (Γ point); (b) total and partial density of states.

coupling (SOC) could induce a band gap decrease of about 0.35 eV and 1.13 eV for B = Sn and Pb, respectively.

As SOC is known to be important for modeling electronic properties of heavier elements,[44] the electronic structure properties of all orthorhombic (MA)BX_3 (B = Sn, Pb; X = F, Cl, Br, I) perovskites are further calculated by GGA + SOC. As an example, Fig. 3 shows the calculated band structure as well as the total and partial density of states (DOS) of (MA)$PbCl_3$, while that of the rest of the seven systems are provided in Fig. S2–S8 of the ESI.†

From Fig. 3(a) and S2(a)–S8(a),† the direct band gap nature of semiconductors is confirmed in these perovskites with their valence band maxima and conduction band minima located at the Γ point of the Brillouin zone. Table 4 summarizes our calculated band gaps of orthorhombic (MA)BX_3 (B = Sn, Pb; X = F, Cl, Br, I) perovskites, which are in good agreement with available theoretical results of (MA)PbI_3 and (MA)SnX_3 (X = Cl, Br, and I).[1,17,32,33] Comparing with the GGA + PBE calculations without including SOC (2.685 eV for (MA)$PbCl_3$) shown in Fig. S9 of the ESI,† a much lower band gap (1.614 eV) was obtained (but still stay as direct band-gap semiconductors) which is consistent with the band-gap decrease predicted by Lang *et al.*[5] In addition, the contribution of the p-orbitals is much lower when SOC is included. The calculated band gap values in Table 4 do show some deviations from the experimental data, with the results from the calculations including SOC being farther from experiment in most cases. Although the absolute values of the calculated band gaps vary with the adopted methods, their shifting trends when altering metal cations or halogen anions in these perovskites stays the same. The band gaps become smaller as large halogen and/or metal ions are included in the (MA)BX_3 structure as shown in Table 4, with the two most extreme cases of (MA)SnI_3 and (MA)PbF_3. When substituting Sn with Pb in B sites, larger band gaps are received for (MA)BX_3 with the same type of halogen.

From the total DOS (TDOS) and the partial DOS (PDOS) for each element in the (MA)BX_3 shown in Fig. 3(b) and S2(b)–S8(b),† it suggests that methyl ammonium ion contributes little

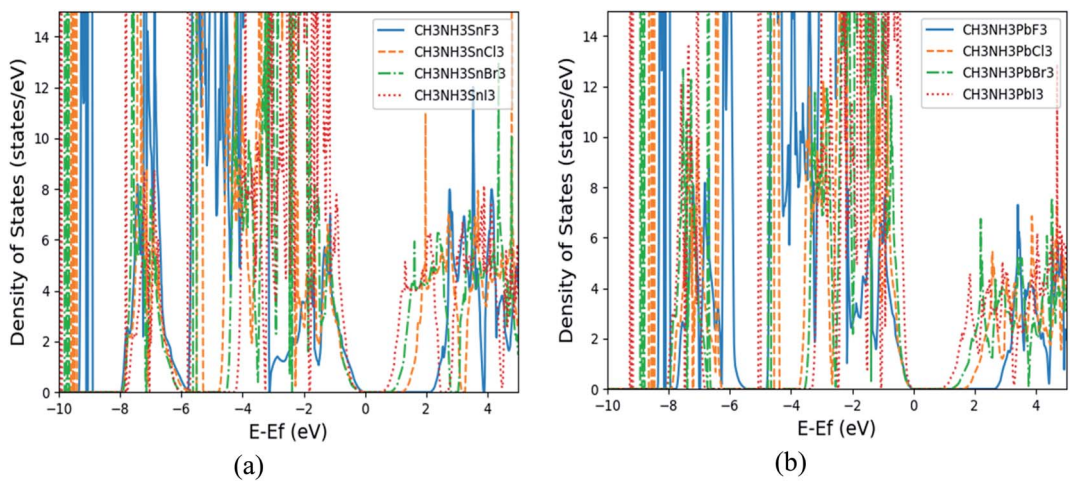

Fig. 4 The calculated total density of states (TDOS) of (MA)SnX_3 (a) and (MA)PbX_3 (b).

to the region around the Fermi level. Taking (MA)$PbCl_3$ as an example, the halogen Cl p-orbital contributes primarily to the valence band (VB) and the metal p-orbital to the conduction band (CB), as shown in the subpanels of Fig. 3(b). Cl has its p-orbital PDOS shifted to further above the Fermi energy, moving the relevant perovskites' CBs in the same manner. Conversely, larger halogens appear to shift the CB closer to the Fermi energy (note: possibly by raising the Fermi energy). Drifting away from the Fermi energy enlarges the band gap, which explains why these two types of perovskites (*i.e.*, (MA)SnI_3 and (MA)PbF_3) have the smallest and largest band gaps, respectively, as shown in the TDOS comparison in Fig. 4. Compared to available literature trends, *e.g.* (MA)SnI_3 *versus* (MA)PbI_3, our results do match well with the literature.[33]

Based on the electronic structural properties, the formation energies (E_{form}) of orthorhombic (MA)BX_3 (B = Sn, Pb; X = F, Cl, Br, I) perovskites are evaluated by

$$E_{form,ABX} = E_{0,ABX} - E_{0,AX} - E_{0,BX} \quad (3)$$

where $E_{0,ABX}$ refers to the energy of a particular perovskite per formula unit as listed in Table 1, $E_{0,AX}$ refers to the energy per formulation of the (MA)X salt formed from the relevant halogen of the perovskite, and $E_{0,BX}$ refers to the energy per formulation of the BX_2 salt formed from the relevant halogen and metal of the perovskite. The calculated $E_{0,AX}$ and $E_{0,BX}$ are listed in Table S8 of the ESI.† AX and BX_2 are important to reference against when quantifying thermodynamic stability as they are the phases typically in thermodynamic equilibrium with ABX_3 perovskites. The calculated E_{form} of (MA)BX_3 perovskites are given in Table 4. The formation energy of all perovskites of (MA)BX_3 is negative in their orthorhombic phase, with an exception of (MA)SnF_3. This suggests that all seven perovskites could exist in *Pnma* phase, including the least studied (MA)PbF_3. Unlike (MA)SnF_3, whose formation energy is positive, *Pnma* phase (MA)PbF_3 perovskite could be favorable under low temperature conditions, although this has not yet been discovered experimentally to our best knowledge. To further verify the stability, additional computational work on the phonon properties of these fluorine-containing perovskites is needed to examine the stability and dynamics of their crystal structures.

3.3 Optical properties

To study the optical properties, the frequency-dependent dielectric matrix in the long wavelength limit ($q \rightarrow 0$) can be calculated using the sum over states approach.[45] A brief description of our calculation methods is summarized here while detailed can be found in our previous publications.[46–49] The formula for the imaginary part of the dielectric constant is a 3 × 3 Cartesian tensor:

$$\varepsilon_2{}^{\alpha\beta} = \frac{4\pi^2 e^2}{\Omega} \lim_{q\to 0} \frac{1}{q^2} \sum_{c,v,k} 2\omega_k \delta(\varepsilon_{ck} - \varepsilon_{vk} - \omega) \times \left\langle u_{ck+\varepsilon_\alpha q} | u_{vk} \right\rangle \left\langle u_{ck+\varepsilon_\beta q} | u_{vk} \right\rangle^* \quad (4)$$

where the summation is over indices c (CB states), v (VB states), and k (k-points). e is elementary charge, Ω is volume of the Brillouin zone, ω_k is weight of the k-point vector, ε_{ck} and ε_{vk} are energy levels, u_{ck} is the periodic portion of the orbital at k-point k. Vector e_α is made of unit vectors for the Cartesian directions and α/β refer to axis x, y, and z. From the imaginary part, the real part can be obtained by a Kramers–Kronig transformation.

$$\varepsilon_1{}^{\alpha\beta} = 1 + \frac{2}{\pi} P \int_0^\infty \frac{\varepsilon_2^{\alpha\beta}(\omega')\ \omega'}{\omega'^2 - \omega^2} d\omega' \quad (5)$$

By including SOC, Fig. 5 shows the calculated $\varepsilon_1{}^{\alpha\beta}$ and $\varepsilon_2{}^{\alpha\beta}$ *versus* wavelength for (MA)SnX_3 (X = F, Cl, Br, I). The results of (MA)PbX_3 (X = F, Cl, Br, I) are shown in Fig. S10 of the ESI.† Due to the symmetrical and isotropic features of these crystals, the off-diagonal elements of dielectric tensor are zero and the diagonal elements (ε^{xx}, ε^{yy}, ε^{zz}) are close to each other, but not identical. As shown in Fig. 5, we take the average of these three diagonal elements as the overall dielectric constants in further

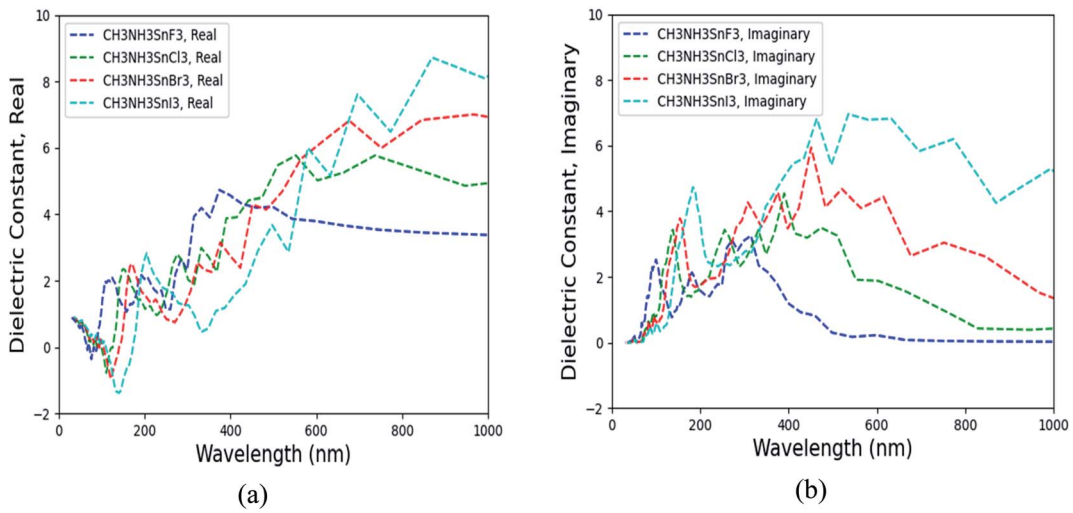

Fig. 5 The calculated dielectric matrix of (MA)SnX_3 perovskites by taking the average of diagonal elements (ε^{xx}, ε^{yy}, ε^{zz}). (a) Real part ε_1, (b) imaginary part ε_2.

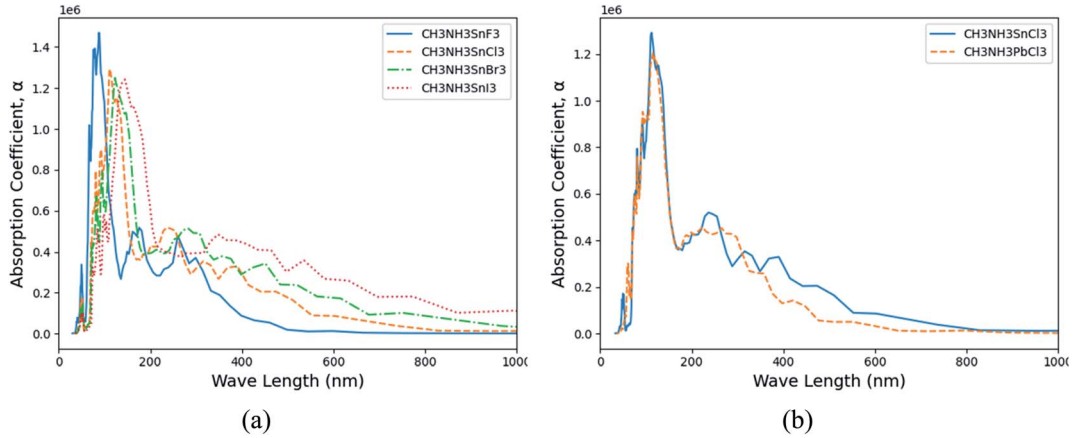

Fig. 6 The calculated absorption coefficient (α) *versus* frequency in wavelength. (a) (MA)SnX_3 (X = F, Cl, Br, I); (b) (MA)BCl_3 (B = Sn, Pb).

calculation of their optical properties. Comparing Fig. 5 with the results of the GGA + PBE calculations without including SOC shown in Fig. S11,† the main difference is seen in the imaginary dielectric constant, for which the heavier halogen perovskites do not fall off as quickly against wavelength.

As promising candidate materials in optical sensor applications, the most interesting wavelength range is from ultraviolet (UV) (10–400 nm) through the visible spectrum (400–800 nm) to near infrared and infrared (IR) (>800 nm), particularly, around the visible and near infrared range (~400 to 1000 nm).[46] As shown in Fig. 5 and S9,† with halogen anions varying from F to I, both real and imaginary parts of the dielectric matrix in the frequency range of 400–1000 nm are increased. Other optical properties (*e.g.*, the index of refraction, extinction coefficient, reflectivity, optical conductivity, absorption coefficient) derived from the dielectric matrix change correspondingly. According to eqn (4) and (5), the dielectric matrix depends on the differences of CB and VB states. When the halogen anion changes from F to I, the band gap of (MA)BX_3 is decreased, as shown in Table 4. The small band gap slows down the decay of the imaginary portion of the dielectric constant. Therefore, (MA)SnI_3 possesses higher ${\varepsilon_2}^{\alpha\beta}$ over (MA)SnF_3 with longer wavelength, as shown in Fig. 5. Similarly, when substituting Sn for Pb, the corresponding (MA)PbX_3 possesses a higher band gap as shown in Table 4 and hence its dielectric matrix is smaller in comparison with that of (MA)SnX_3. Comparing Fig. 5 with Fig. S10,† at visible light wavelength range (>400 nm), (MA)SnI_3 has the highest ${\varepsilon_1}^{\alpha\beta}$ and ${\varepsilon_2}^{\alpha\beta}$ values while (MA)PbF_3 possesses the lowest ${\varepsilon_2}^{\alpha\beta}$ and ${\varepsilon_2}^{\alpha\beta}$, which are consistent with trends of their electronic properties as described in Section 3.2.

Based on the calculated ${\varepsilon_1}^{\alpha\beta}$ and ${\varepsilon_2}^{\alpha\beta}$ values from eqn (4) and (5), the absorption coefficient, α, is further calculated at a particular wavelength, λ, as shown in eqn (6).

$$\alpha = \frac{2\sqrt{2\pi}}{\lambda}\left(\left(-\varepsilon_1 + \left({\varepsilon_1}^2 + \varepsilon_2\right)^2\right)^{\frac{1}{2}}\right)^{\frac{1}{2}} \quad (6)$$

where c refers to the speed of light. Other optical properties (*e.g.*, index of refraction, extinction coefficient, reflectivity, optical conductivity, *etc.*) also can be derived from dielectric matrix and are provided in the ESI.† The calculated absorption coefficients of (MA)SnX_3 and (MA)PbX_3 are shown in Fig. 6(a) and S12 of the ESI,† respectively. Notably from these figures, perovskites containing heavier halogen anions exhibit higher absorption coefficients, particularly in the visible light range (400–800 nm) – a key parameter for both optical sensor and photovoltaic cell applications. Such shifts are a directly reflection of the change trends on their electronic structure properties. Despite Pb-containing perovskites' prevalence over Sn counterparts, (MA)BCl_3 (B = Sn, Pb) as an example, the Sn-containing perovskites display a higher absorption coefficient in the visible light range, as shown in Fig. 6(b). This suggests another important benefit the Sn-based perovskites could contribute to the performance improvement in the aforementioned applications besides their environmental benign advantages over the Pb-based counterparts.

Other optical properties such as extinction coefficient, index of refraction, and reflectivity are also calculated with detailed results placed in Fig. S13–S19 of the ESI.† From these results, similar change trends are also observed when varying the X site anions of perovskites from F to I and/or substituting Sn with Pb cations in the B sites. Hence, to achieve better optical performance (*e.g.*, higher absorption coefficient) among orthorhombic perovskites (MA)BX_3 (B = Sn, Pb; X = F, Cl, Br, I), our results suggest that (MA)SnX_3 are better candidates than (MA)PbX_3. Overall, with the same metal (Sn or Pb) cations, iodine anion contributes the strongest optical absorption among all halogen types while fluorine makes the least. As for high optical absorption performance in the visible light range, we predict that (MA)SnI_3 is the best candidate while (MA)PbF_3 is least favorable. However, (MA)PbF_3, if stable, could serve in UV detection applications for its strong adsorption in the 10–400 nm range.

4. Conclusions

In this work, the electronic and optical properties of orthorhombic (MA)BX_3 (B = Sn, Pb; X = F, Cl, Br, I) perovskites were calculated by first-principles density functional theory. The structures were relaxed to obtain the energy-minimized

geometry and formation energies. The bulk modulus was evaluated by fitting the Birch–Murnaghan equation-of-state and in good agreement with available data. Deviations from literature structure simulations exist, but a definite trend is still observed. Notably, the $(MA)PbF_3$ perovskite is found to have a negative formation energy, indicating its possible presence at low temperature conditions. The electronic structures of all eight perovskite systems were analyzed to evaluate the band gaps and contributors to the band gaps, with electronegativity suspected to be a major driving factor. Variations in the p-orbitals of the halogen anions is believed to decide the different levels in the valence band of these perovskite systems, and that of the metal cations contributing to the conduction band level. Hence, the band gaps of $(MA)BX_3$ are decreased with halogen element X varying from F to I, and larger band gaps are found in $(MA)PbX_3$ than corresponding $(MA)SnX_3$. Our calculations on the optical properties of these orthorhombic perovskites show the adsorption enhancement in the visible light range when the halogen anions vary from F to I, so does the substitution of Pb with Sn cation in the B sites, reflecting the similar trends as in the partial DOS shifting. Tin-based halide perovskites (particularly $(MA)SnI_3$) are shown to – among those examined – have comparably better absorbance of visible light energy, suggesting additional benefits in their replacement of the lead-based counterparts in broad perovskites applications.

Conflicts of interest

There are no conflicts to declare.

Acknowledgements

S. N. thanks the Department of Energy, Mickey Leland Energy Fellowship (MLEF) for the Summer Internship at National Energy Technology Laboratory (NETL) as well as the Louisiana Board of Regents (LBR) for supporting his research through the LBR Graduate Fellowship. T. J. thanks the NETL Research and Innovation Center (R&IC) for providing Computational resources administered by the Oak Ridge Institute for Science and Education (ORISE). S. W. thanks Louisiana Harrelson Family Professorship for supporting this research. Revision computations were performed on computational resources provided by the Louisiana Optical Network Infrastructure (LONI). This report was prepared as an account of work sponsored by an agency of the United States Government. Neither the United States Government nor any agency thereof, nor any of their employees, makes any warranty, express or implied, or assumes any legal liability or responsibility for the accuracy, completeness, or usefulness of any information, apparatus, product, or process disclosed, or represents that its use would not infringe privately owned rights. Reference herein to any specific commercial product, process, or service by trade name, trademark, manufacturer, or otherwise does not necessarily constitute or imply its endorsement, recommendation, or favoring by the United States Government or any agency thereof. The views and opinions of authors expressed herein do not necessarily state or reflect those of the United States Government or any agency hereof.

References

1 T. Baikie, Y. Fang, J. M. Kadro, M. Schreyer, F. Wei, S. Mhaisalkar, M. Graetzel and T. J. White, *J. Mater. Chem. A*, 2013, 5628–5641.
2 G. M. Dalpian, Q. Liu, C. C. Stoumpos, A. P. Douvalis, M. Balasubramanian, M. G. Kanatzidis and A. Zunger, *Phys. Rev. Mater.*, 2017, **1**, 1–10.
3 J. H. Noh, S. H. Im, J. H. Heo, T. N. Mandal and S. I. Seok, *Nano Lett.*, 2013, **13**, 1764–1769.
4 C. Eames, J. M. Frost, P. R. F. Barnes, B. C. O'Regan, A. Walsh and M. S. Islam, *Nat. Commun.*, 2015, **6**, 2–9.
5 L. Lang, J. H. Yang, H. R. Liu, H. J. Xiang and X. G. Gong, *Phys. Lett. A*, 2014, **378**, 290–293.
6 R. Prasanna, T. Leijtens, S. P. Dunfield, J. A. Raiford, E. J. Wolf, S. A. Swifter, J. Werner, G. E. Eperon, C. de Paula, A. F. Palmstrom, C. C. Boyd, M. F. A. M. van Hest, S. F. Bent, G. Teeter, J. J. Berry and M. D. McGehee, *Nat. Energy*, 2019, **4**, 939–947.
7 S. Ruan, J. Lu, N. Pai, H. Ebendorff-Heidepriem, Y.-B. Cheng, Y. Ruan and C. R. McNeill, *J. Mater. Chem. C*, 2018, **6**, 6988–6995.
8 X. Yang, Y. Gao, Z. Ji, L. B. Zhu, C. Yang, Y. Zhao, Y. Shu, D. Jin, Q. Xu and W. W. Zhao, *Anal. Chem.*, 2019, **91**, 9356–9360.
9 G. Kakavelakis, E. Gagaoudakis, K. Petridis, V. Petromichelaki, V. Binas, G. Kiriakidis and E. Kymakis, *ACS Sens.*, 2018, **3**, 135–142.
10 F. Hao, C. C. Stoumpos, D. H. Cao, R. P. H. Chang and M. G. Kanatzidis, *Nat. Photonics*, 2014, **8**, 489–494.
11 A. Jaffe, Y. Lin, C. M. Beavers, J. Voss, W. L. Mao and H. I. Karunadasa, *ACS Cent. Sci.*, 2016, **2**, 201–209.
12 T. Oku, in *Solar Cells – New Approaches and Reviews*, ed. L. A. Kosyachenko, InyechOpen, 2015, pp. 77–101.
13 N. Onodayamamuro, T. Matsuo and H. Suga, *J. Phys. Chem. Solids*, 1990, **51**, 1383–1395.
14 D. Weber, *Z. Naturforsch., B: J. Chem. Sci.*, 1978, **33**, 1443–1445.
15 M. Afsari, A. Boochani and F. Shirdel, *Optik*, 2019, **199**, 163360.
16 A. O. Al Ghaithi, S. A. Aravindh, M. N. Hedhili, T. K. Ng, B. S. Ooi and A. Najar, *ACS Omega*, 2020, **5**, 12313–12319.
17 I. O. A. Ali, D. P. Joubert and M. S. H. Suleiman, *Eur. Phys. J. B*, 2018, **91**, 263.
18 C. Bernal and K. S. Yang, *J. Phys. Chem. C*, 2014, **118**, 24383–24388.
19 K. T. Butler, J. M. Frost and A. Walsh, *Mater. Horiz.*, 2015, **2**, 228–231.
20 D. O. Demchenko, N. Izyumskaya, M. Feneberg, V. Avrutin, U. Ozgur, R. Goldhahn and H. Morkoc, *Phys. Rev. B*, 2016, **94**, 075206.
21 Y. Q. Huang, J. Su, Q. F. Li, D. Wang, L. H. Xu and Y. Bai, *Phys. B*, 2019, **563**, 107–112.
22 R. Lindblad, N. K. Jena, B. Philippe, J. Oscarsson, D. Q. Bi, A. Lindblad, S. Mandal, B. Pal, D. D. Sarma, O. Karis, H. Siegbahn, E. M. J. Johansson, M. Odelius and H. Rensmo, *J. Phys. Chem. C*, 2015, **119**, 1818–1825.

23 A. Maalej, Y. Abid, A. Kallel, A. Daoud, A. Lautie and F. Romain, *Solid State Commun.*, 1997, **103**, 279–284.
24 J. S. Park, S. Choi, Y. Yan, Y. Yang, J. M. Luther, S. H. Wei, P. Parilla and K. Zhu, *J. Phys. Chem. Lett.*, 2015, **6**, 4304–4308.
25 S. Park, Y. S. Seo, C. W. Ahn, W. S. Woo, J. Kyhm, S. A. Lee, I. W. Kim and J. Hwang, *J. Phys. D: Appl. Phys.*, 2019, **52**, 335302.
26 L. P. Peng, Y. Hu and L. Xu, *Sci. Adv. Mater.*, 2016, **8**, 2223–2230.
27 L. P. Peng and L. Xu, *Sci. Adv. Mater.*, 2018, **10**, 1519–1527.
28 P. Umari, E. Mosconi and F. De Angelis, *Sci. Rep.*, 2014, **4**, 4467.
29 L. J. Wu, Y. Q. Zhao, C. W. Chen, L. Z. Wang, B. Liu and M. Q. Cai, *Chin. Phys. B*, 2016, **25**, 107202.
30 M. Zhong, W. Zeng, H. Tang, L. X. Wang, F. S. Liu, B. Tang and Q. J. Liu, *Sol. Energy*, 2019, **190**, 617–621.
31 C. Li, J. Wei, M. Sato, H. Koike, Z. Z. Xie, Y. Q. Li, K. Kanai, S. Kera, N. Ueno and J. X. Tang, *ACS Appl. Mater. Interfaces*, 2016, **8**, 11526–11531.
32 Y. Wang, T. Gould, J. F. Dobson, H. M. Zhang, H. G. Yang, X. D. Yao and H. J. Zhao, *Phys. Chem. Chem. Phys.*, 2014, **16**, 1424–1429.
33 J. Feng and B. Xiao, *J. Phys. Chem. C*, 2014, **118**, 19655–19660.
34 G. Kresse and J. Furthmuller, *Comput. Mater. Sci.*, 1996, **6**, 15–50.
35 G. Kresse and J. Furthmuller, *Phys. Rev. B: Condens. Matter Mater. Phys.*, 1996, **54**, 11169–11186.
36 G. Kresse and J. Hafner, *Phys. Rev. B: Condens. Matter Mater. Phys.*, 1993, **47**, 558–561.
37 P. E. Blochl, *Phys. Rev. B: Condens. Matter Mater. Phys.*, 1994, **50**, 17953–17979.
38 J. P. Perdew, M. Ernzerhof and K. Burke, *J. Chem. Phys.*, 1996, **105**, 9982–9985.
39 A. Jain, S. P. Ong, G. Hautier, W. Chen, W. D. Richards, S. Dacek, S. Cholia, D. Gunter, D. Skinner, G. Ceder and K. A. Persson, *APL Mater.*, 2013, **1**, 011002.
40 J. Feng and B. Xiao, *J. Phys. Chem. Lett.*, 2014, **5**, 1278–1282.
41 Y. Duan, *Phys. Rev. B: Condens. Matter Mater. Phys.*, 2008, **77**, 045332.
42 F. Chiarella, A. Zappettini, F. Licci, I. Borriello, G. Cantele, D. Ninno, A. Cassinese and R. Vaglio, *Phys. Rev. B: Condens. Matter Mater. Phys.*, 2008, **77**, 045129.
43 I. Borriello, G. Cantele and D. Ninno, *Phys. Rev. B: Condens. Matter Mater. Phys.*, 2008, **77**, 235215.
44 P. Mavropoulos, I. Galanakis, V. Popescu and P. H. Dederichs, *J. Phys.: Condens. Matter*, 2004, **16**, S5759–S5762.
45 M. Gajdos, K. Hummer, G. Kresse, J. Furthmuller and F. Bechstedt, *Phys. Rev. B: Condens. Matter Mater. Phys.*, 2006, **73**, 045112.
46 Y. Duan, P. Ohodnicki, B. Chorpening and G. Hackett, *J. Solid State Chem.*, 2017, **256**, 239–251.
47 T. Jia, P. Ohodnicki, B. Chorpening, J. Lekse, G. Hackett and Y. Duan, *Phys. Chem. Chem. Phys.*, 2019, **21**, 26117–26122.
48 T. Jia, Z. Zeng, H. Q. Lin, Y. Duan and P. Ohodnicki, *RSC Adv.*, 2017, **7**, 38798–38804.
49 Y. N. Wu, W. A. Saidi, J. K. Wuenschell, T. Tadano, P. Ohodnicki, B. Chorpening and Y. Duan, *J. Phys. Chem. Lett.*, 2020, **11**, 2518–2523.